Anchor name	Description	Sequence	Source/citation
trLAT	Transmembrane domain from human LAT. mEos3.2 fused on the C terminus.	N’-MEEAILVPCVLGLLLLPILAMLMALCVHCHRLPGSGIH-[mEos3.2]-C’	Ilya Levental Lab [1]
trLATo	Transmembrane domain from mouse LAT. mEos3.2 fused on the N terminus. Also contains an N-terminal ER translocation signal.	N’-[ER]-ARDPPVAT-[mEos3.2]-FSRMEADALSPVGLGLLLLPFLVTLLAALCVRCRELPVS-C’	Jonathan Grover – Akira Ono Lab
trLAT-P	Identical to trLATo with the palmitoylation site at C27 mutated to A.	N’-[ER]-ARDPPVAT-[mEos3.2]-FSRMEADALSPVGLGLLLLPFLVTLLAAL**A**VRCRELPVS-C’	Jonathan Grover – Akira Ono Lab
trLAT-2P	Identical to trLATo with both palmitoylation sites at C27 and C30 mutated to A.	N’-[ER]-ARDPPVAT-[mEos3.2]-FSRMEADALSPVGLGLLLLPFLVTLLAAL**A**VR**A**RELPVS-C’	Jonathan Grover – Akira Ono Lab [2]
trLATm1 (PtoL)	Same TMD as trLAT with mEos3.2 fused to the N terminus and with prolines P8 and P17 in the LAT transmembrane domain mutated to L.	N’-[mEos3.2]-FSSSSFEFMEEAILVLCVLGLLLLLILAMLMALCVHCHRLPGSGSTGSR-C’	Ilya Levental Lab [3]
trLATm2 (allL+A)	Same TMD as trLAT with mEos3.2 fused to the N terminus and with residues within the transmembrane domain mutated to L and A. This modification increases the TMD interfacial surface area with the membrane [3].	N’-[mEos3.2]-FSSSSFEFMEELLALLLLALAAAALLALLALLACVHCHRLPGSGSTGSR-C’	Ilya Levental Lab [3]
trCD4 (trLAT/CD4)	Transmembrane domain from CD4, contains 2 palmitoylation sites. mEos3.2 fused on the C terminus.	N’-MEEVQPMALIVLGGVAGLLLFIGLGIFFCVHCHRLPGSGIH-[mEos3.2]-C’	Ilya Levental Lab [3]
trCD4o	Transmembrane domain from CD4, contains 2 palmitoylation sites. mEos3.2 fused on the N terminus.	N’-[mEos3.2]-FSSSSFEFMESNIKVLPTWSTPVQPMALIVLGGVAGLLLFIGLGIFFCVRCRHRRRQGSTGSR-C’	Sarah Veatch Lab (unpublished)
trPAG	Transmembrane domain from PAG/CSK, contains 2 palmitoylation sites. mEos3.2 fused on the C terminus.	N’-MQITLWGSLAAVAIFFVITFLIFLCSSCHRLPGSGIH-[mEos3.2]-C’	Ilya Levental Lab [3]
trCD45	Transmembrane domain from CD45. mEos3.2 fused on the N terminus.	N’-[mEos3.2]-SRGTMMTPNESTNFNAKALIIFLVFLIIVTSIALLVVLYKIYDLRKKRADPPDLDN-C’	Sarah Veatch Lab (unpublished)
M	N terminus of Src with 1 myristoylation and short polybasic sequence.	N’-MGSSKSKPKDPSQRRNNNNGPVAT-[mEos3.2]-C’	William Rodgers Lab [4]
PM	N terminus of Lyn with 1 myristoylation and 1 palmitoylation.	N’-MGCIKSKRKDKDLELKLRILQSTVPRARDPPVAT-[mEos3.2]-C’	Barbara Baird and David Holowka Lab [5]
PPM	N terminus of Fyn with 1 myristoylation and 2 palmitoylations.	N’-MGCVQCKDKE-[mEos3.2]-C’	Akira Ono Lab [6]
GG	C terminus of KRas with polybasic sequence and original farnesylation replaced by geranylgeranylation.	N’-[mEos3.2]-FRSDGKKKKKKSKTKCQLL-C’	Barbara Baird and David Holowka Lab [5]
FP	C terminus of NRas with 1 farnesylationand 1 palmitoylation.	N’-[mEos3.2]-FSSSSLNSAVDGCMGLPCVVM-C’	John Hancock Lab [7]
FPP	C terminus of HRas with 1 farnesylation and 2 palmitoylations.	N’-[mEos3.2]-FSSSSLNSGCMSCKCVLS-C’	John Hancock Lab [7]
GPI	C-terminal sequence derived from CD58 encoding a GPI-attachment signal.	N’-[mEos3.2]-YGGNGSGQHQYDPRPSSGHSRHRYALIPIPLAVITTCIVLYMNVL-C’	Kai Simons Lab [8]

Supplementary Table 1: Sequence, design, and origin information for anchor constructs. Descriptions, sequences, sources and references (if available) are provided for the anchor constructs used in this study. For GPMV measurements, cells expressed anchors conjugated to either GFP, YFP, or RFP, as described in the original publications. For fluorescence localization measurements, anchors are conjugated to mEos3.2. The full sequence of mEos3.2 is omitted in the table but listed below. Some anchor constructs contain ER translocation signal sequences that improve delivery to the plasma membrane. The ER translocation signal sequence is also omitted from the table but is listed below. Underlined sections of sequences represent portions taken from the native protein. Other parts of the sequence are linkers or overhangs used for cloning.

mEos3.2 sequence [mEos3.2]:
MSAIKPDMKIKLRMEGNVNGHHFVIDGDGTGKPFEGKQSMDLEVKEGGPLPFAFDILTTAFHYGNRVFAKYPDNIQDYFKQSFPKGYSWERSLTFEDGGICNARNDITMEGDTFYNKVRFYGTNFPANGPVMQKKTLKWEPSTEKMYVRDGVLTGDIEMALLLEGNAHYRCDFRTTYKAKEKGVKLPGAHFVDHCIEILSHDKDYNKVKLYEHAVAHSGLPDNARR
ER translocation sequence [ER]: MELFWSIVFTVLLSFSCRGSDWESLQSTVPR

Construct name	Description	Sequence	Source/citation
trCD28cr-eGFP	Minimal “co-receptor” with the non-palmitoylated transmembrane domain of CD28 and intracellular eGFP tag.	N’-[GM-CSF]-[scFV]-[STII]-[G4S]-[IgG4]-MFWVLVVVGGVLACYSLLVTVAFIIFWVRSKRSRGGHSDTGAT-[eGFP]-C’	Stanley Riddell lab[9]
trCD4cr-eGFP	Minimal “co-receptor” with the palmitoylated transmembrane domain of CD4 and intracellular eGFP tag.	N’-[GM-CSF]-[scFV]-[STII]-[G4S]-[IgG4]-MALIVLGGVAGLLLFIGLGIFFCVRCRHRRRQKRGRKKLLYIFTGAT-[eGFP]-C’	Stanley Riddell lab[9]

Supplementary Table 2: Sequence, design, and origin information for minimal co-receptor constructs. Descriptions, sequences, sources and references are provided for the minimal “co-receptor” constructs used in this study. Underlined sections of sequences represent portions taken from the native protein. Other parts of the sequence are linkers or overhangs used for cloning. Sequences for some constituent elements of the constructs including leader sequences and sequences of CD19-specific scFV, Strep-tagII, IgG4 hinge, and eGFP are given below.

Granulocyte-macrophage colony-stimulating factor leader sequence [GM-CSF]: MLLLVTSLLLCELPHPAFLLIP

Anti-CD19 single chain variable fragment sequence [scFV]:
DIQMTQTTSSLSASLGDRVTISCRASQDISKYLNWYQQKPDGTVKLLIYHTSRLHSGVPSRFSGSGSGTDYSLTISNLEQEDIATYFCQQGNTLPYTFGGGTKLEITGSTSGSGKPGSGEGSTKGEVKLQESGPGLVAPSQSLSVTCTVSGVSLPDYGVSWIRQPPRKGLEWLGVIWGSETTYYNSALKSRLTIIKDNSKSQVFLKMNSLQTDDTAIYYCAKHYYYGGSYAMDYWGQGTSVTVSS

Strep tag II sequence [STII]: NWSHPQFEK

2x G4S linker [G4S]: GGGGSGGGGS

IgG4 hinge sequence [IgG4]: ESKYGPPCPPCP

eGFP sequence [eGFP]:
MVSKGEELFTGVVPILVELDGDVNGHKFSVSGEGEGDATYGKLTLKFICTTGKLPVPWPTLVTTLTYGVQCFSRYPDHMKQHDFFKSAMPEGYVQERTIFFKDDGNYKTRAEVKFEGDTLVNRIELKGIDFKEDGNILGHKLEYNYNSHNVYIMADKQKNGIKVNFKIRHNIEDGSVQLADHYQQNTPIGDGPVLLPDNHYLSTQSALSKDPNEKRDHMVLLEFVTAAGITLGMDELYKL

Supplementary Figure 1: Considering finite time-intervals (τ) improves counting statistics and corrects for cross-talk between imaging channels.

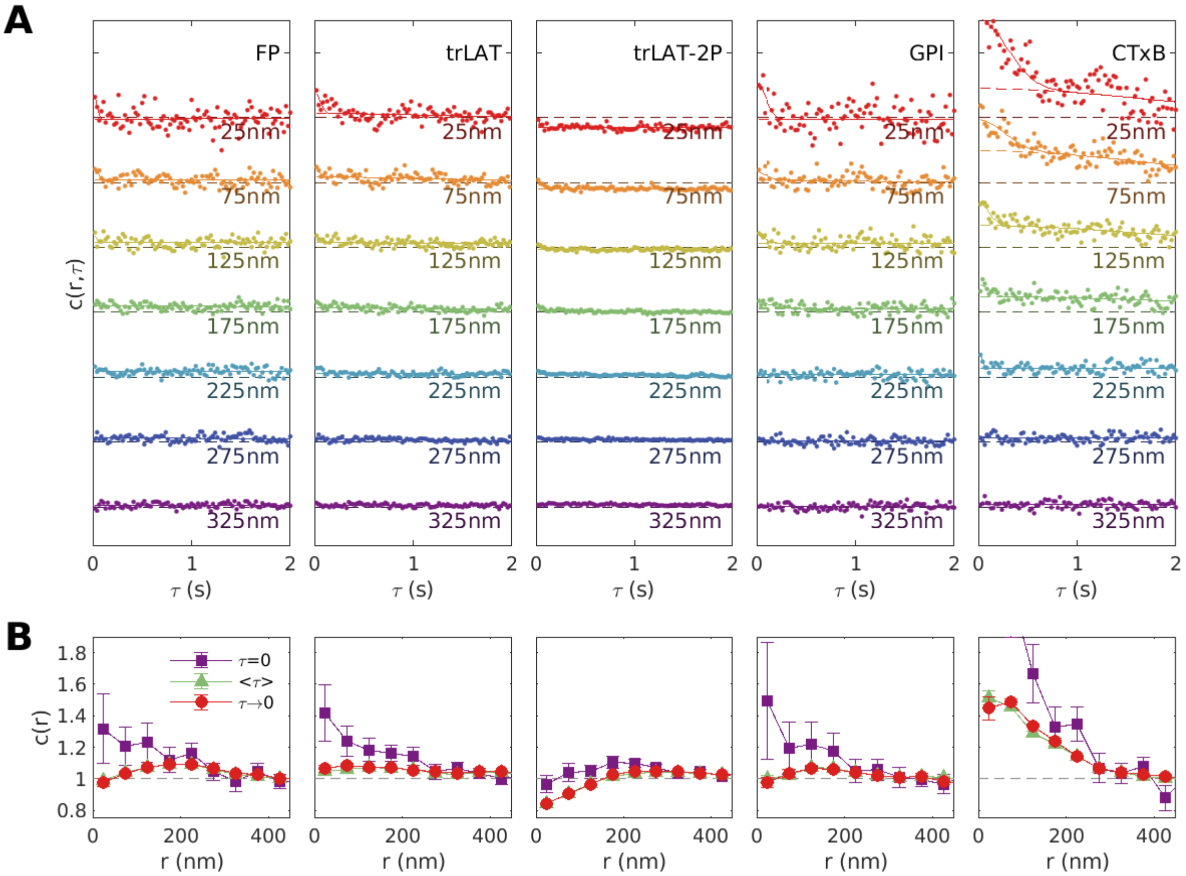

a, Raw c(τ) for bins separated at the specified r values tabulated from single representative cells viewed 2-10min after BCR crosslinking. Points are fit to a superposition of two Gaussian functions (solid lines) to capture amplitude variation that occurs on distinct time-scales. We interpret long-time variation as arising from slow motions of BCR clusters. Short-time variation is due to bleed-through between color channels and its range is bounded by probe diffusion time through a diffraction limited area. This bleed-through effect is most prominent for CTxB because this is the only anchor probed that is labeled with an organic fluorophore (Cy3B), which is brighter than mEos3.2 and bleeds more into the SiR (far red) emission channel. CTxB is also the slowest anchor probed, so bleed-through extends to larger τ. Bleed-through is corrected by extrapolating the long-range Gaussian fit to τ→0 (dashed colored lines). Since these curves are determined by many points (~100), the extrapolated to τ→0 value is determined with smaller error bounds than for any given c(τ=0) point. **b,** Cross-correlation curves c(r) for the same examples shown in **a**. The curve labeled τ=0 assembles the value of the τ=0 points with error-bars deriving from Poisson counting statistics within individual spatial bins. These curves do not correct for bleed-through and have large error bounds. The curve labeled <τ> presents the mean and SEM of points tabulated for τ<2s, while the curve labeled τ→0 extrapolates the slow Gaussian fit to τ=0 (where colored dashed line intersects y axis in **a**) and error bars represent the 68% confidence interval in this extrapolation. These curves represent 2 methods of improving statistics and correcting bias arising from bleed-through. These curves are similar, and have lower amplitudes and reduced errors compared to c(r, τ=0).

Supplementary Figure 2: Temporal evolution of correlation function amplitudes.

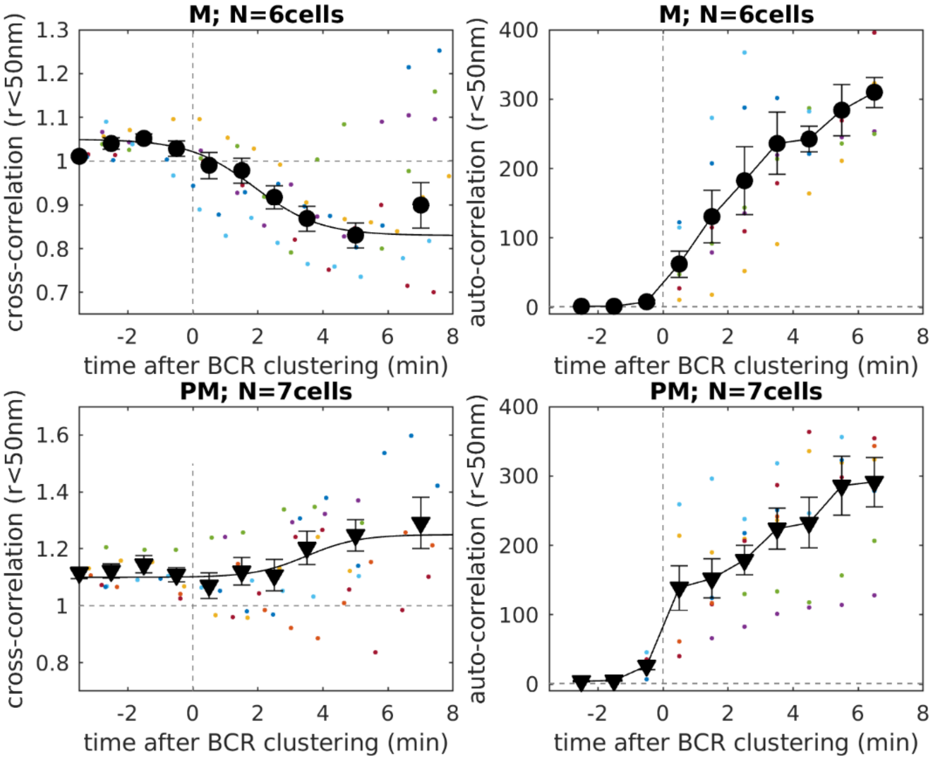

Data points (small colored points) and average curves (filled black symbols) showing cross-correlation amplitudes between BCR and the specified anchors (c(r<50nm, τ->0s); left) or auto-correlations amplitudes of BCR at τ=0.5s (g(r<50nm, τ=0.5s); right) every 1min using a sliding 2 min time-window. For c(r), points are tabulated with the same number of image frames (4000) at intervals of 2000 frames, which roughly corresponds to the timing above but is asynchronous across cells. Large symbols represent the mean and SEM of values within 1 min time bins. For g(r), intervals are divided into time bins with a slightly different number of image frames, so points are synchronous, and error bars represent the SEM of points corresponding to the same time. For c(r), error bars represent the SEM of points after binning into 1min intervals (<5min after BCR clustering) or 2min intervals (>5min after BCR clustering).

Supplementary Figure 3: Distribution of corrected cross-correlation amplitudes across cells for all anchors included in this study.

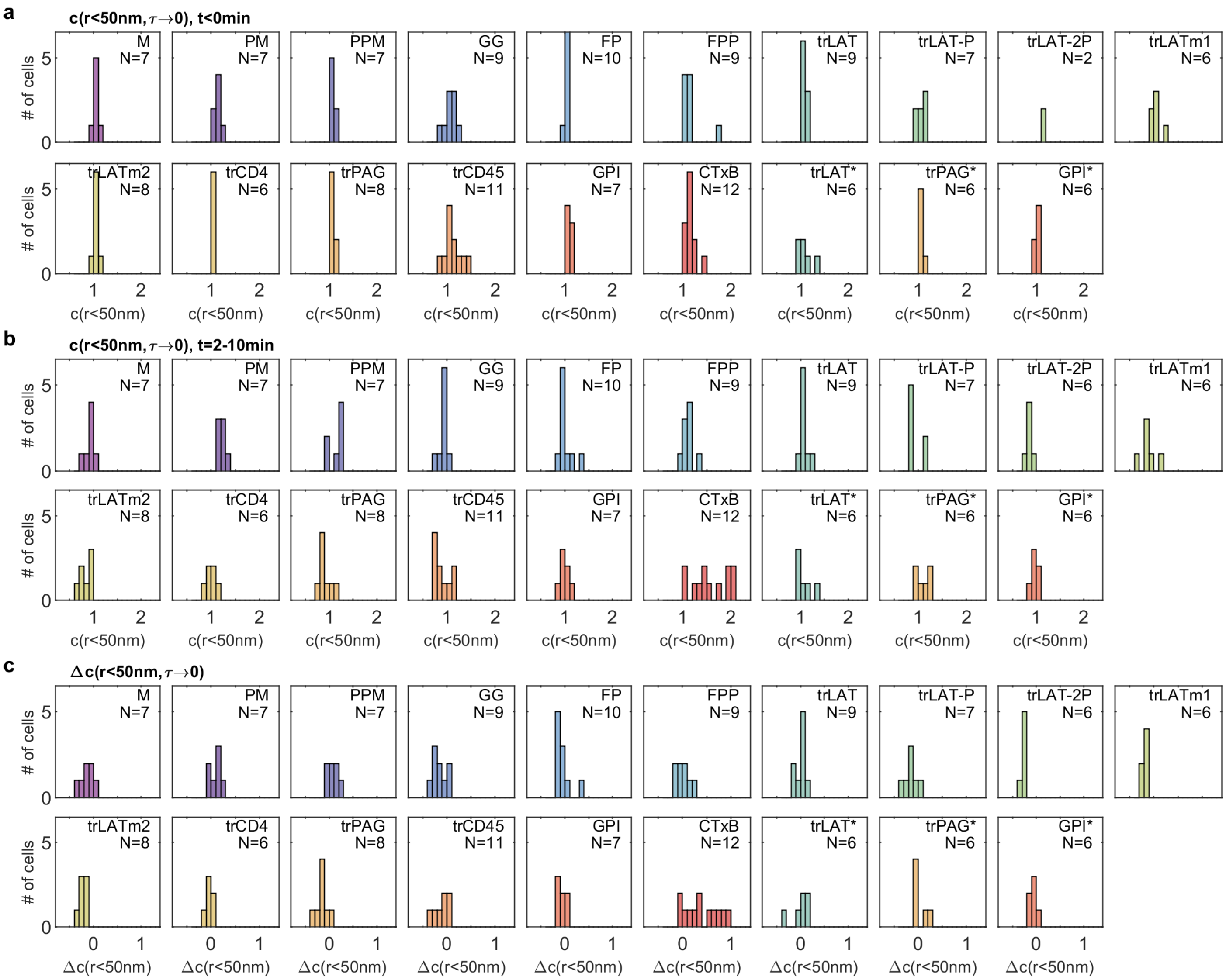

a,b, Cell-to-cell variation in cross-correlation amplitudes c(r<50nm) tabulated from images acquired prior to BCR clustering (**a**, t<0min) and from images acquired t=2-10min after BCR clustering (**b**). **c,** Cell-to-cell variation in the change in correlations after crosslinking (Δc(r)) obtained by subtracting values in **a** from those shown in **b** on a cell by cell basis. N represents the total number of cells examined for each anchor. For trLAT-2P, not all cells were imaged prior to crosslinking. In this case Δc(r) is obtained by subtracting the average value for the cells expressing this anchor that were imaged prior to BCR clustering. Anchor labels ending in * indicate that values are from experiments where BCR was clustered in the presence of 5μM PP2.

Supplementary Figure 4: Anchor expression does not significantly impact BCR cluster size or density.

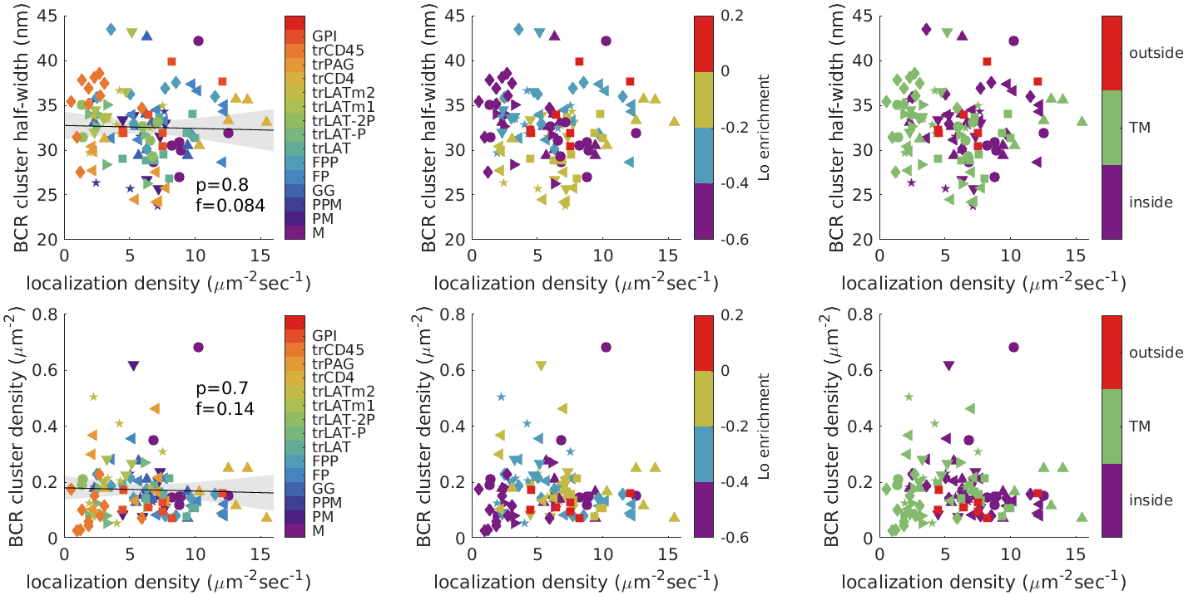

Average BCR cluster size (top) and BCR cluster density (bottom) does not correlate with an estimate of expression level for cells expressing membrane anchored probes. The left most panels show points representing single cells colored by probe identity, the middle panels color points according to the Lo phase partitioning of anchors in GPMVs, and the right panels color points according to anchor class. Fits of all points (shown on left panels) to a linear model are not significantly different from the null hypothesis of zero correlation (left panels). p-values shown are obtained from a two-sided hypothesis test (lower values indicate greater significance), and the f-statistic reports how well the variance in the data is described by the linear fit (higher values indicate greater significance). Gray shaded regions indicate a 95% confidence interval of the linear fit.

Supplementary Figure 5: **Anchor expression does not significantly impact BCR activation.**

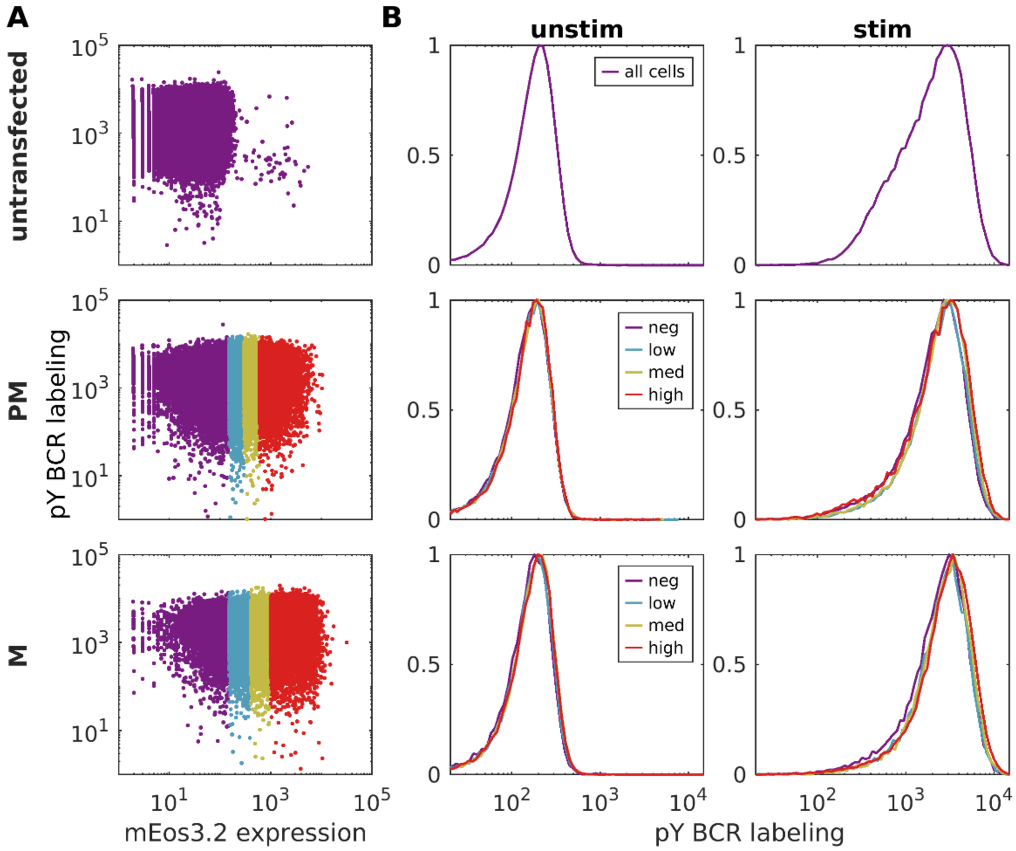

CH27 cells were transfected with mEos3.2 anchor constructs via the same procedures used for imaging. Cells were either left unstimulated or were stimulated by BCR crosslinking for 6 min at room temperature, then fixed and stained with AlexaFluor 647-conjugated antibodies specific to a phosphorylated tyrosine at Tyr182 on an ITAM of the CD79A subunit of BCR. **a,** Phosphorylated BCR (pBCR) labeling vs. mEos3.2 expression for single cells that are untransfected (top) or transfected with PM-mEos3.2 (middle) or M-mEos3.2 (bottom) constructs. For PM and M transfected cells, a threshold is applied based on the background fluorescence signal of untransfected cells to identify mEos3.2-positive cells. Positive cells are then divided into 3 levels of anchor expression comprising the bottom, middle, and top 1/3 of expressing cells, presented as different colored points on the scatter plots. **b,** Normalized histograms of pBCR labeling for either untransfected cells or transfected cells divided into mEos3.2 negative, low-expressing, medium-expressing, or high-expressing groups using the scheme shown in **a**. Cells are unstimulated (left) or stimulated by BCR crosslinking (right).

Supplementary Figure 6: Probe enrichment at BCR clusters does not correlate with BCR cluster properties for all anchors but GPI.

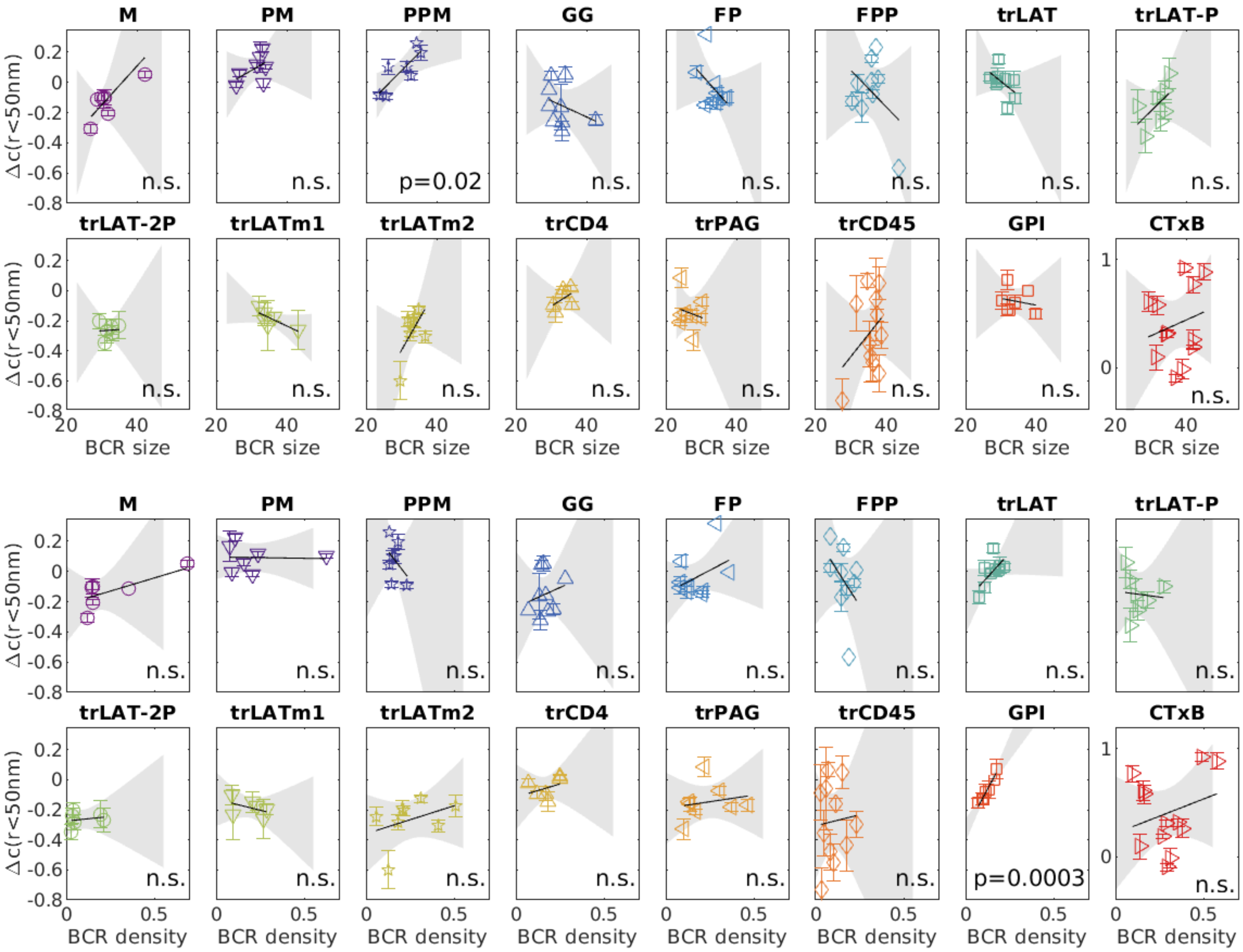

Enrichment in BCR clusters (Δc(r<50nm) as a function of average BCR cluster size (top) and average BCR cluster density (bottom) evaluated from BCR auto-correlation functions. Points show the mean and 68% confidence interval error estimates of c(r<50nm) from single cells. The number of cells in each group are provided in Supplementary Figure 3. Trends are fit to a linear model. Gray shaded regions indicate a 95% confidence interval of the linear fit and p-values shown are obtained from a two-sided hypothesis test and no adjustments were made for multiple comparisons. Most cases yield insignificant correlations (n.s. corresponding to p>0.05), except for PPM which shows weakly significant correlations with BCR cluster size (p=0.02). This is not considered significant in light of the presence of multiple comparisons. Highly significant correlations are found between GPI enrichment and BCR cluster density (p=0.0003). This correlation for GPI may indicate specific interactions between the anchor and proteins on the cell surface, possibly contributing to this anchor being an outlier in Fig. 2c.

Supplementary Figure 7: Density enrichment of probes with respect to BCR cluster centers as estimated through deconvolution.

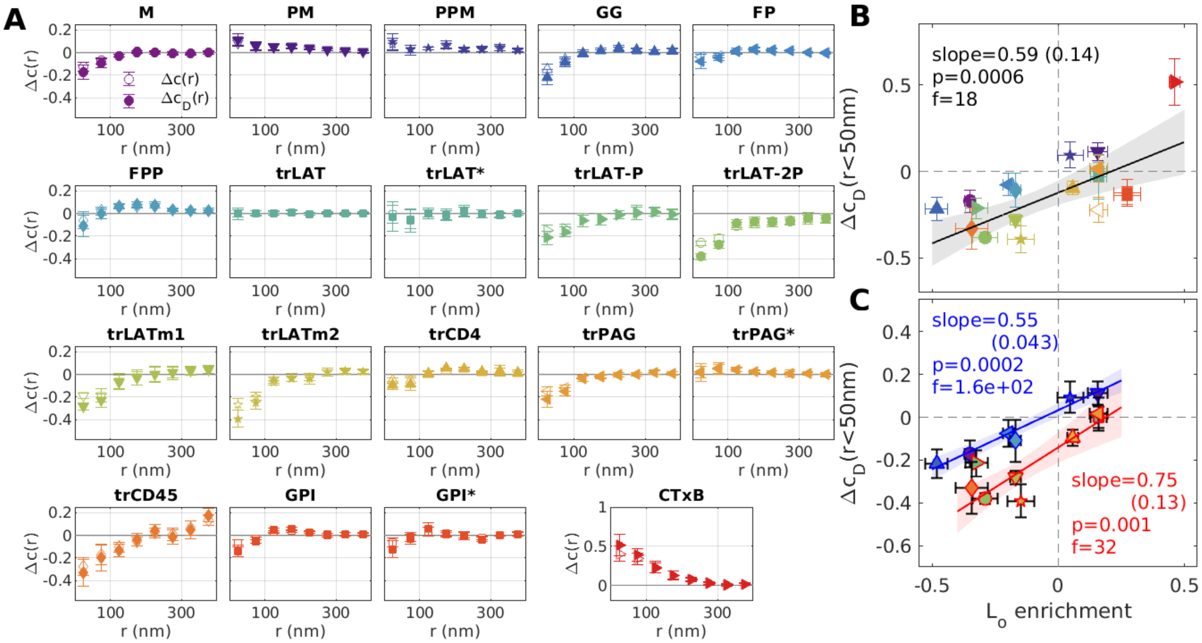

a, Experimentally determined ($\Delta c(r)$; open symbols) and an estimate of anchor density with respect to BCR cluster centers ($\Delta c_D(r)$; closed symbols) obtained by deconvolving $\Delta c(r)$ with a Gaussian function with a standard deviation of 50nm as described in Supplementary Note 1. Points are means and SEM over multiple cells, and cell numbers for each condition are shown in Supplemental Figure 3. **b,** Points are mean and SEM of $\Delta c_D(r<50\text{nm})$ replotted from **a** vs. means and SEM of Lo enrichment in GPMVs replotted from Fig. 2b. **c,** Subset of points replotted from **b**. Points representing inner leaflet peripheral anchors (blue edges) and transmembrane anchors (red edges). Trends in **b**, **c** are fit to a linear model and the significance is assessed with a p-value of the two-sided hypothesis test against the hypothesis of no correlation (lower values indicate greater significance), and an f-statistic that reports how well the variance in the data is described by the linear fit (higher values indicate greater significance). No adjustments were made for multiple comparisons. Shaded regions in **b**,**c** indicate the 95% confidence interval of the linear fit.

Supplementary Figure 8: trCD28cr partitions with the Ld phase in GPMVs.

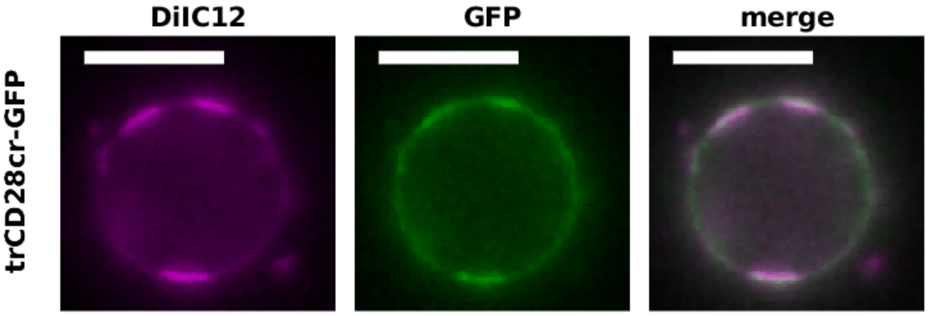

Representative GPMV derived from RBL-2H3 cells expressing trCD28cr-GFP imaged alongside DiIC12, which marks the Ld phase Quantification over 20 vesicles yields a Lo enrichment of -0.32±0.04. Scale-bar is 10µm.

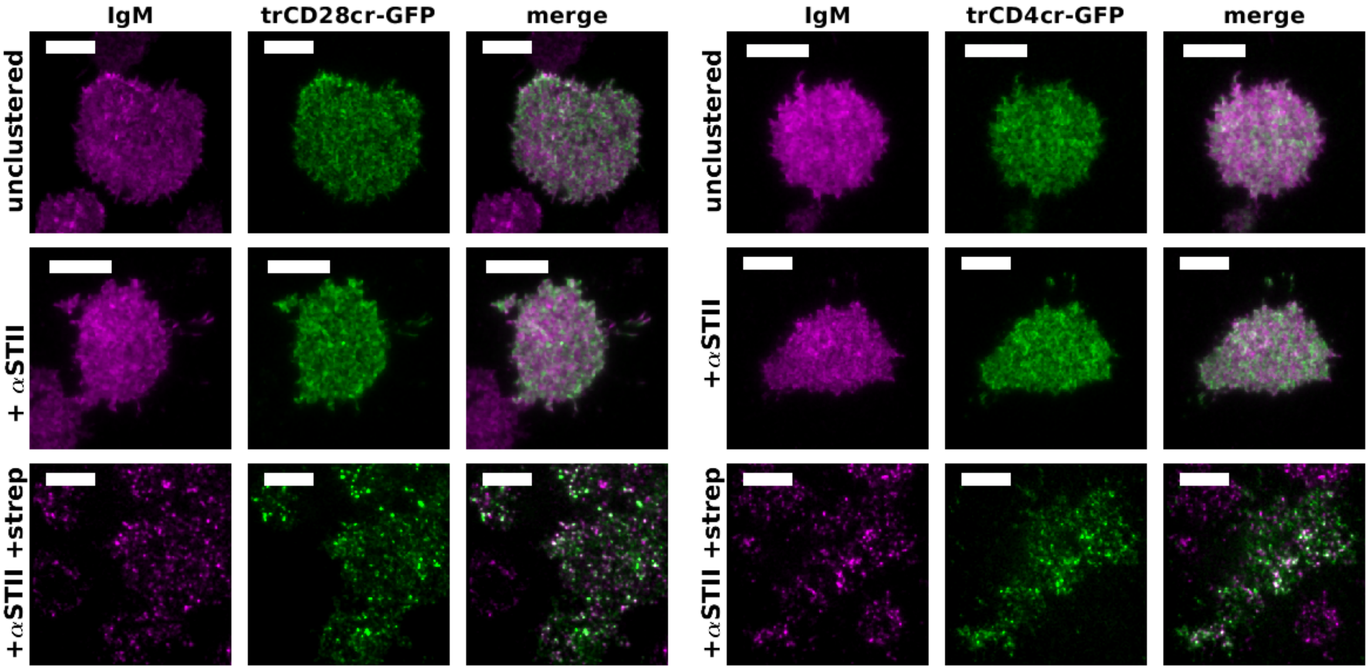

Supplementary Figure 9: Co-crosslinked minimal co-receptors co-localize with BCR puncta. Representative TIRF images of CH27 B cells transduced with either trCD28cr-GFP (left) or trCD4cr-GFP (right). IgM BCR is labeled with biotin-SiR-Fab αIgMμ. Images were taken before additional labeling (top row), after labeling with biotinylated anti Strep-tagII primary antibodies (middle row), and after subsequent co-ligation with biotin-SiR-Fab αIgMμ labeled BCR using streptavidin (bottom row). Both BCR and minimal co-receptors form puncta that co-localize in transduced cells. Individual puncta exhibit a distribution of relative co-receptor and BCR intensities. In all cases, cells shown are representative of >30 cells imaged for each condition. All scale-bars are 10μm.

Supplementary Figure 10: Distribution of corrected cross-correlation amplitudes across cells for co-receptor and alcohol measurements from Figure 3.

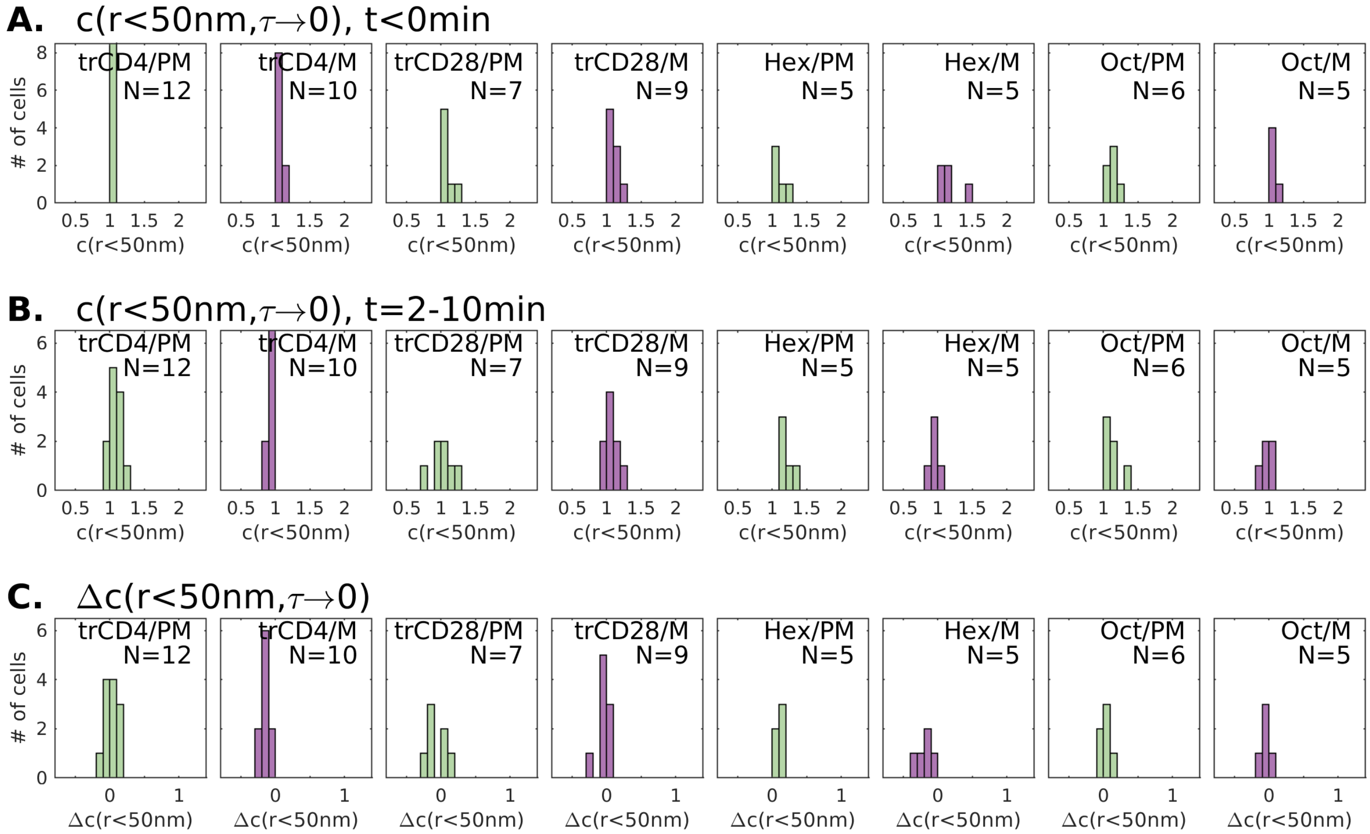

a,b, Cell-to-cell variation in cross-correlation amplitudes c(r<50nm) tabulated from images acquired prior to BCR clustering (**a**, t<0min) and from images acquired t=2-10min after BCR clustering (**b**). **c,** Cell-to-cell variation in the change in correlations after crosslinking (Δc(r)) obtained by subtracting values in A from those shown in B. N represents the total number of cells examined for each condition.

Supplementary Figure 11: BCR cluster properties for measurements reported in Figure 3.

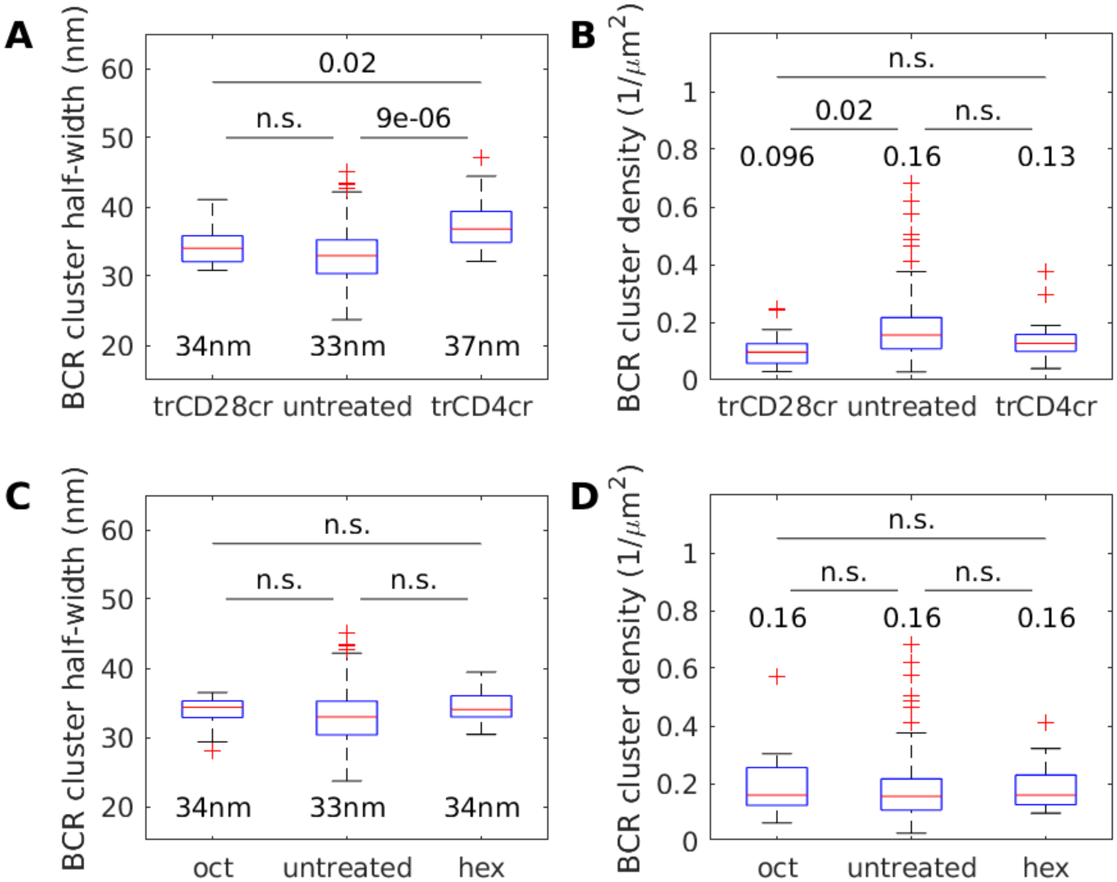

BCR cluster size (**a,c**) and cluster density (**b,d**) as evaluated from BCR autocorrelation functions. On each box, the central mark indicates the median, and the bottom and top edges of the box indicate the 25th and 75th percentiles, respectively. The whiskers extend to the most extreme data points not considered outliers. Outliers are plotted individually using the '+' symbol. The numerical value of the median is written either below (**a,c**) or above (**b,d**) the box. For all comparisons, significance is evaluated using a 2-tailed t-test. The "untreated" category contains all measurements from Fig. 1 (excluding those with pp2 treatment). The number of cells in each category are: 16 (with trCD28cr), 22 (with trCD4cr), 11 (with octanol), 10 (with hexadecanol), and 125 (untreated). Note that the stimulation conditions differ for co-receptor, alcohol treated, and untreated cells, as described in Methods. Briefly, Fab labeling of IgM BCR was less saturated in cells expressing co-receptors (labeled with 1µg/ml in a,b vs. 5µg/ml SiR biotin Fab αIgMµ in c,d and untreated). This was done to ensure incorporation of minimal co-receptors within labeled BCR clusters and likely contributes to the slightly lower median surface density of clusters observed in samples with co-receptors compared to untreated in **b**. Also, the median BCR cluster size for cells with co-receptors is slightly larger than control cells in **a** likely because clusters incorporate unlabeled minimal co-receptors. Alcohol treated cells in **c,d** were imaged on VCAM-1 coated surfaces to improve topography and alcohols were added in DMSO (0.25%). These treatments did not produce significant changes in BCR cluster size or density compared to untreated cells imaged on glass in the absence of DMSO.

Supplementary Figure 12: Spatiotemporal auto-correlation functions (g(r,τ)) and extracted fit parameters for several cells and anchors.

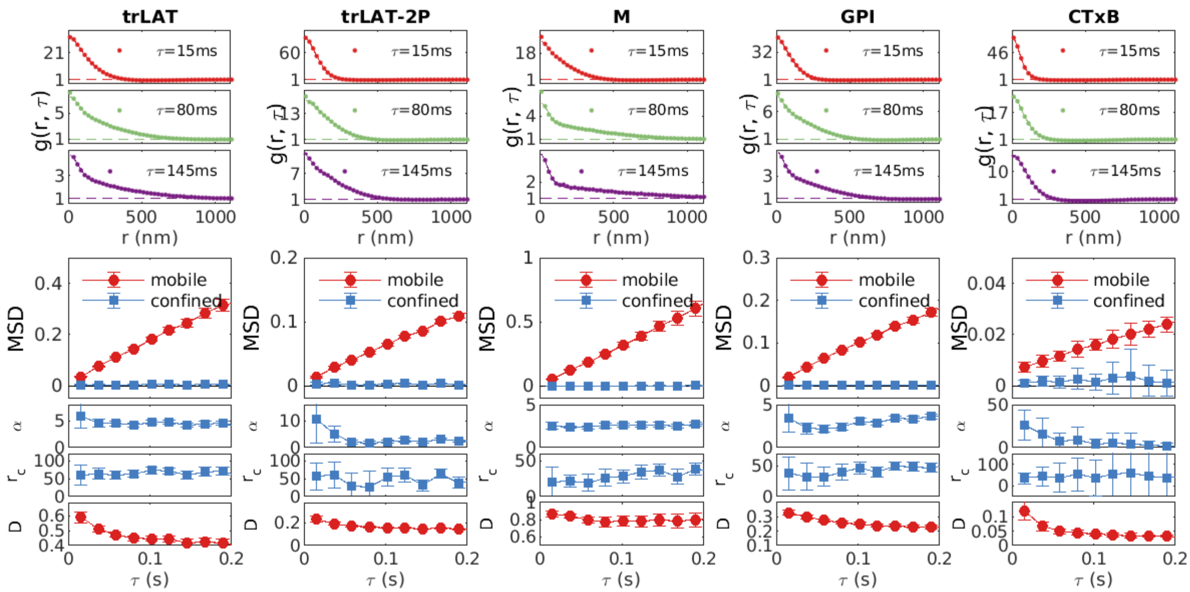

(Top) Spatiotemporal auto-correlation functions, g(r,τ), for single cells expressing the indicated anchors tabulated from localized single molecules acquired between 2-10 min after BCR clustering. The three g(r) curves shown correspond to the indicated time-intervals, with a frame-time of close to 20ms. Points represent measured values and lines are fit to a superposition of 2 Gaussian functions. (Bottom) Mean squared displacements (MSDs) and the percentage of molecules in the more confined state (α) determined by fitting g(r,τ) to superposition of 2 Gaussian functions as described in Supplementary Note 1. Points represent the best fit solution for the single cell shown above and error bounds report on 68% confidence intervals of best fit parameter values. Individual MSDs for the confined (slow) component can be converted to a confinement radius: $r_c = \sqrt{MSD}$ shown here in units of nm. The MSD for the mobile (fast) component is converted to a diffusion coefficient D, with units of μm^2/s as described in Supplementary Note 1.

Supplementary Figure 13: Parameters used to generate the membrane in Figure 5.

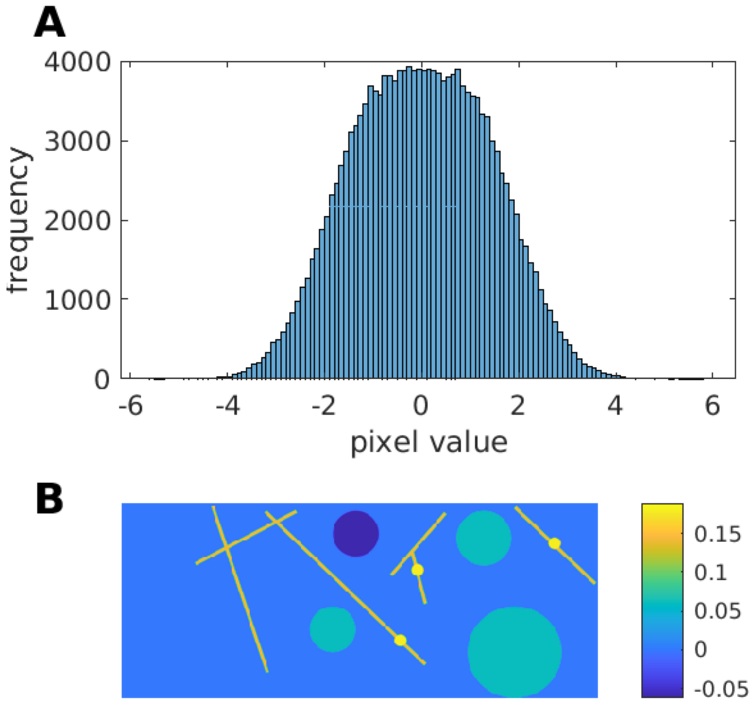

a, The distribution of pixel values used. Half of the values are normally distributed around -1 and half of the values are normally distributed around +1 to create the broad distribution shown. **b**, Image representation of the applied field matrix. Most values are set to 0.

Supplementary Figure 14: Flow cytometry gating strategy for representative examples.

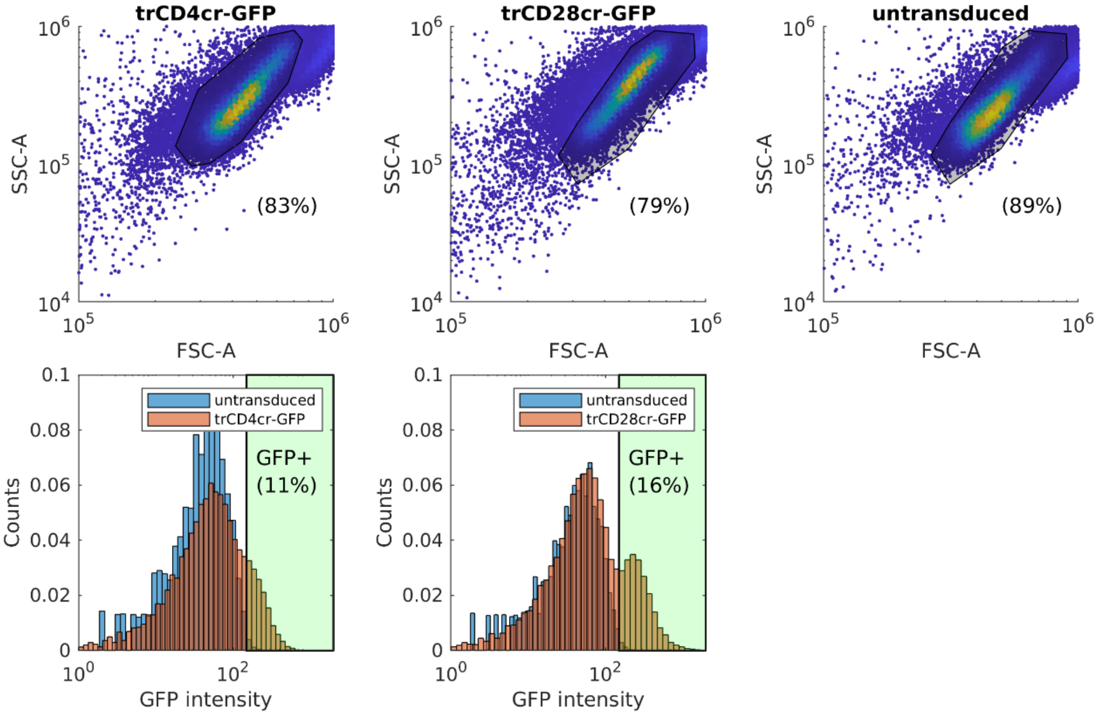

(Top) Single healthy cells were selected by gating on side-scatter and forward scatter signals as shown. 75-90% of total cells were typically selected at this step, and exact values for these examples are indicated on the plots. (Bottom) For measurements involving transduced cells, expressing cells were gated on eGFP intensity. This population represents 10-20% of the total population of forward and side-scatter gated cells.

Supplementary Note 1: Description of algorithms used for analysis of single molecule localizations.

Cross-correlation analysis

Steady-state cross-correlations from live cells were calculated as described previously[10], with minor modifications. In brief, cross-correlation functions, c(r ,τ), were computed from localizations in each channel that occurred in the same frame or in frames separated by a time interval τ. Long-range gradients in labeling density arising from diffusing molecules entering the TIR field along with the complicated boundary condition generated by the mask are accounted for through normalization as follows. For each channel, images reconstructed from data acquired over the entire steady-state time window are convoluted with a Gaussian kernel with σ = 1 µm and masked using the same binary mask applied to localization data. The cross-correlation of the blurred, masked images from each channel is calculated using FFTs and radially averaged as described in[10–12] and is used as a normalization factor for c(r ,τ). This treatment filters structure larger than 1 µm in size from the steady-state cross-correlation function.

Bleed-through effects are evident at short τ, and this contribution is removed by fitting c(r ,τ) to a sum of two Gaussian functions for each value of r:

$$\mathrm{c}_{\mathrm{observed}}(\mathrm{r}\,,\tau) = 1 + \mathrm{A}_{\mathrm{narrow}} \exp\left(-\frac{\tau^2}{4\sigma_{narrow}^2}\right) + \mathrm{A}_{\mathrm{broad}} \exp\left(-\frac{\tau^2}{4\sigma_{broad}^2}\right)$$

The standard deviation of the narrow Gaussian function, σ_{narrow}^2, is constrained by how long it takes an anchor to diffuse across a diffraction limited distance (taken to be 250nm). This assumes that BCR is less mobile than anchors, which is consistent with experimental observations especially after BCR clustering. The broader Gaussian is interpreted to capture the more slowly varying envelope of the actual c(r, τ), most likely due to slow motions of BCR clusters. Bleed-through is accounted for by excluding the amplitude of the narrow Gaussian function to yield the values reported in the main text:

$$\mathrm{c(r)} = \mathrm{c(r,\tau \to 0)} = 1 + \mathrm{A}_{\mathrm{broad}}(r)$$

Several examples of this fitting procedure are shown in Supplementary Figure 1. This bleed-through correction is not applied for the stimulation-time dependent curves of Fig 1b. For these measurements, the reported values are simply an average over 2s in τ:

$$\mathrm{c(r)} = \langle \mathrm{c(r,\tau)} \rangle_{\tau<2s}$$

This improves statistics while reducing the impact of bleed-through in data with reduced signal to noise and produces results that are very similar to the bleed-through calculation described above, as shown in Supplementary Figure 1. We note that the bleed-through correction assumes that any correlations occurring on timescales relevant to anchors diffusing through a diffraction limited spot arise from crosstalk between imaging channels. As a result, our methods are not sensitive to real correlations occurring on this or shorter timescales.

Since we consistently observe subtle enrichment of anchors with respect to BCR in cells prior to BCR crosslinking (Supplementary Figure 2 and Extended Data Figure 3), which we attribute to long-lived membrane topography, we report on the enhanced enrichment of probes upon BCR crosslinking in order to isolate the impact of BCR clustering. This is done by subtracting $\mathrm{c(r,\tau \to 0)}$ obtained from images acquired prior to BCR crosslinking (t<0) from those acquired between 2-10 min after BCR crosslinking (t=2-10).

$$\Delta c(r) = c_{t=2-10}(r,\tau \to 0) - \ c_{t<0}(r,\tau \to 0)$$

Δc is tabulated for each cell, and the variance reported in Δc represents the standard error of the mean averaged over cells. For one anchor, trLAT-2P, images were not acquired prior to BCR crosslinking for some cells included in the dataset. In this case, we subtracted the average $c_{t<0}(r,\tau \to 0)$ obtained from cells where this data was present from $c_{t=2-10}(r,\tau \to 0)$ for individual cells.

Deconvolution of Δc(r)

Both resolution and the finite size of BCR clusters blur the measured Δc(r), reducing the dynamic range. Deconvolution was accomplished by first spreading Δc(r) over angles to get an angularly symmetric two dimensional $\Delta c(\vec{r})$ and a blurring function was estimated as a 2D Gaussian function with standard deviation of 50nm, representing the size of BCR clusters (35nm) and the approximate localization precision of mEos3.2 (35nm) added in quadrature. The 2D deconvolution was accomplished using the deconvlucy function in Matlab, using the blurring function as the point spread function, then $\Delta c_D(\vec{r})$ was averaged over angles to produce $\Delta c_D(r)$. The same blurring function was used for all cells even though there is some cell-to-cell variation in localization precision and average BCR cluster size to simplify the analysis. A more careful correction would involve a rigorous estimate of the type and magnitude of noise from each cell and a blurring function specific to each measurement, which was not done here. The average $\Delta c_D(r)$ curves were tabulated by averaging over $\Delta c_D(r)$ obtained from individual cells. We note that while the dynamic range of these curves increases in magnitude, so does the standard error of the mean between cells at short separation distances.

Auto-correlation analysis and extracting BCR cluster properties

Auto-correlation functions g(r, τ) were tabulated from localized positions as a function of radius r and time interval τ for each cell imaged and normalized following the same protocol as for cross-correlations described above. g(r, τ) functions were tabulated for localizations acquired between 2 and 10 min after activation unless otherwise specified. Unlike the cross-correlation, g(r, τ) contains intensity arising from multiple observations of single molecules because most fluorophores are observed over multiple sequential image frames. This can be used to quantify the diffusion of anchors following methods described under the heading "Quantification of anchor mobility in cells" below.

In order to characterize the size and density of BCR clusters, as reported in Figure 1 and Extended Data Figure 1, g(r,τ) was fit to $g(r,\tau) = A\exp\left\{-r^2/4\sigma^2\right\}$ at fixed τ to extract the amplitude (A) and range (σ) of correlations. At short τ, g(r,τ) is dominated by signals originating from the same molecules, and reports largely on the localization precision of the measurement. At longer τ, the range of correlations reflects the size of BCR clusters and the motion of these clusters. BCR cluster size is estimated by fitting g(r,τ) at a τ=0.1s, which is longer than the typical on-time of a SiR fluorophore, but before BCR clusters have moved more than several nm (Extended Data Fig. 1c). To obtain an estimate of BCR cluster density (ρ), we apply the relation $A = 1/(4\pi\sigma^2\rho)$[11], which makes the assumption that correlations are dominated by laterally organized clusters at this time-separation (τ=0.1s).

Quantification of anchor mobility in cells:

The motion of membrane anchors was quantified from localized single molecule positions from g(r, τ) as described previously[10] and summarized in Supplementary Figure 12. At each τ, the normalized g(r, τ) was fit to a superposition of two Gaussian functions to extract two distinct mean squared displacements according to the relation:

$$g(r) - 1 = \frac{A_1}{\pi R_1^2} exp\{-r^2/R_1^2\} + \frac{A_2}{\pi R_2^2} exp\{-r^2/R_2^2\}$$

The mean squared displacement (MSD) for each component is related to the fit parameters R_1 and R_2 which are determined at each τ:

$$MSD_1(\tau) = R_1^2 - 2\langle\sigma_{LP}^2\rangle$$

$$MSD_2(\tau) = R_2^2 - 2\langle\sigma_{LP}^2\rangle$$

Where $\langle\sigma_{LP}^2\rangle$ is the squared localization precision extracted from the single molecule fits and averaged over the complete dataset. The fraction of the population within the first component is $\alpha = A_1/(A_1 + A_2)$.

Several examples of g(r, τ) and fits are shown in Supplementary Figure 12 and the average values of fit parameters for all probes at the shortest time-interval (15ms) are displayed in Fig. 4 and Extended Data Figure 10. We refer to the shorter MSD as the immobile component since it does not increase rapidly with τ. The longer MSD increases roughly linearly with τ, consistent with diffusive motion. We have chosen to fit to only two states for simplicity but it is possible that more mobile states are present, in which case our single mobile MSD can be interpreted as a weighted average of these states. The fraction of the population within the slow component is determined at each τ and is largely independent of τ, with some exceptions (Supplementary Figure 12).

The MSD is related to the diffusion coefficient through the relation $MSD(\tau) = 4D(\tau)\tau$. Since fluorophores are illuminated continuously through a finite integration time, images contain information regarding probe locations at different times throughout the integration window. As a result, the effective τ differs from the frame times of the measurement (τ_o)[13]. This is accounted for as follows:

$$\tau = \tau_o\left(1 - \frac{1}{3}\frac{integration\ time}{\tau_o}\right)$$

The integration time was held constant at 20ms for measurements. The frame rate (the smallest value of τ_o) is slightly larger than the integration time and varies across measurements. This correction is largest for short τ_o when the integration time is almost equivalent to τ_o.

Motions of BCR proximal anchors were isolated from the entire population of anchors by cross-correlating anchor localizations within 100nm of a localized BCR with all anchor localizations. Since BCR clusters are largely immobile after BCR clustering, anchor localizations were included if they passed within 100nm of a BCR localization localized up to 2s previously, which implements the assumption that the BCR cluster remains fixed in space even if a fluorophore labeling BCR is not observed. Cross-correlations of BCR proximal anchors and total anchors were normalized using the same geometrical correction factor used for the cross-correlation of BCR and anchors, since the BCR proximal anchor distribution closely follows that of BCR alone. Spatio-temporal cross-correlation functions were fit to extract mobility parameters following the procedures described above for autocorrelations, with the exception that the confinement radius was held a constant value given to improve the robustness of nonlinear fitting of correlation functions tabulated from fewer localized pairs. The constant value used was the value extracted when fitting the mobility of all anchors in the same cell.

Code to tabulate and interpret cross-correlations and auto-correlations, representative datasets, and several practical examples are available online at https://github.com/VeatchLab/smlm-analysis. These algorithms are explained in depth in a recent publication[14].

References cited

1. Levental, I., Lingwood, D., Grzybek, M., Coskun, U. & Simons, K. Palmitoylation regulates raft affinity for the majority of integral raft proteins. *Proc. Natl. Acad. Sci. U.S.A.* **107**, 22050–22054 (2010).
2. Stone, M. B., Shelby, S. A., Núñez, M. F., Wisser, K. & Veatch, S. L. Protein sorting by lipid phase-like domains supports emergent signaling function in B lymphocyte plasma membranes. *eLife Sciences* **6**, e19891 (2017).
3. Lorent, J. H. *et al.* Structural determinants and functional consequences of protein affinity for membrane rafts. *Nat Commun* **8**, 1219 (2017).
4. Rodgers, W. Making membranes green: construction and characterization of GFP-fusion proteins targeted to discrete plasma membrane domains. *Biotechniques* **32**, 1044–1046, 1048, 1050–1051 (2002).

5. Pyenta, P. S., Holowka, D. & Baird, B. Cross-correlation analysis of inner-leaflet-anchored green fluorescent protein co-redistributed with IgE receptors and outer leaflet lipid raft components. *Biophys J* **80**, 2120–2132 (2001).
6. Ono, A., Waheed, A. A. & Freed, E. O. Depletion of cellular cholesterol inhibits membrane binding and higher-order multimerization of human immunodeficiency virus type 1 Gag. *Virology* **360**, 27–35 (2007).
7. Apolloni, A., Prior, I. A., Lindsay, M., Parton, R. G. & Hancock, J. F. H-ras but Not K-ras Traffics to the Plasma Membrane through the Exocytic Pathway. *Mol Cell Biol* **20**, 2475–2487 (2000).
8. Keller, P., Toomre, D., Díaz, E., White, J. & Simons, K. Multicolour imaging of post-Golgi sorting and trafficking in live cells. *Nat Cell Biol* **3**, 140–149 (2001).
9. Liu, L. *et al.* Inclusion of Strep-tag II in design of antigen receptors for T-cell immunotherapy. *Nat. Biotechnol.* **34**, 430–434 (2016).
10. Stone, M. B. & Veatch, S. L. Steady-state cross-correlations for live two-colour super-resolution localization data sets. *Nat Commun* **6**, (2015).
11. Veatch, S. L. *et al.* Correlation Functions Quantify Super-Resolution Images and Estimate Apparent Clustering Due to Over-Counting. *PLoS ONE* **7**, e31457 (2012).
12. Shelby, S. A., Shaw, T. R. & Veatch, S. L. Measuring the co-localization and dynamics of mobile proteins in live cells undergoing signaling responses. in *The Immune Synapse: Methods and Protocols* (eds. Baldari, C. T. & Dustin, M. L.) vol. 2654 (Humana, 2023).
13. Berglund, A. J. Statistics of camera-based single-particle tracking. *Phys. Rev. E* **82**, 011917 (2010).
14. Shelby, S. A., Shaw, T. R. & Veatch, S. L. Measuring the co-localization and dynamics of mobile proteins in live cells undergoing signaling responses. 2022.10.17.511423 Preprint at https://doi.org/10.1101/2022.10.17.511423 (2022).